Freestanding perovskite and infinite-layer nickelate membranes

Hoshang Sahib,* Laurent Schlur, Nathalie Viart, and Daniele Preziosi†

Université de Strasbourg, CNRS, IPCMS UMR 7504, F-67034 Strasbourg, France

Bernat Mundet, Kumara Cordero, and David Pesquera

Catalan Institute of Nanoscience and Nanotechnology,

ICN2 Campus UAB 08193 Bellaterra, Barcelona, Spain

(Dated: January 6, 2025)

Abstract

Following the discovery of superconductivity in hole-doped $NdNiO_2$ infinite-layer thin films, extensive research has been conducted particularly to compare these materials with cuprates. Superconductivity has also been observed in nickelate thin films with other rare-earth elements such as Pr and La, but not in their bulk forms, suggesting a critical role for substrate-induced strain/interface or dimensionality effects. In this study, we used water-soluble $(Ca,Sr)_3Al_2O_6$ sacrificial layers to fabricate freestanding perovskite nickelate membranes and explore the phase transformation to infinite-layers of the membranes via topotactic reduction in the absence of any template effect from the substrate. Highly metallic $NdNiO_3$ membranes with bulk-like hysteretic metal-to-insulator transitions could be obtained when transferred from a $LaAlO_3$ substrate. The topotactic reduction of these membranes with CaH_2 was shown to be successful as characterized by the expected decrease of the out-of-plane cell parameter and absence of apical oxygens. The reduced membranes however displayed insulating characteristics similar to those of bulk infinite-layer nickelates. Our findings strongly indicate that a template is necessary to stabilize a coherent and robust infinite-layer phase with optimal transport properties.

* hoshang.sahib@ipcms.unistra.fr

† daniele.preziosi@ipcms.unistra.fr

I. INTRODUCTION

Perovskite rare-earth nickelate heterostructures, $R\mathrm{NiO_3}$ (R being a rare-earth), have been the subject of intense theoretical and experimental research efforts. In particular a theoretical proposal assumed that those materials could mimic the high-Tc superconductivity of cuprates[1], for which a Cu-3de_g orbital selective Cooper pairing is believed to be responsible for the zero-resistance state[2]. Recently, soft-chemistry processes using $\mathrm{CaH_2}$ powder as a reducing agent have allowed the stabilization of a superconducting infinite-layer (IL) phase in hole-doped $R\mathrm{NiO_2}$ thin films (with R = Nd, Pr, and La) grown onto $\mathrm{SrTiO_3}$ (STO) substrates[3–5]. The absence of bulk superconductivity, even under pressure[6], highlights the crucial role of substrate-induced strain/interface and/or dimensionality effects in stabilizing the superconducting phase. To date, the nickelate IL phase is stabilized by optimizing the lattice mismatch between the perovskite and IL phases and the substrate. Specifically, the tetragonal IL phase ($a = 0.392\,\mathrm{nm}, c = 0.328\,\mathrm{nm}$ as measured for the undoped bulk compound [7]) is stabilized onto STO ($a = 0.3905\,\mathrm{nm}$), to minimize the lattice mismatch (approximately -0.4%). However, the STO imposes a large tensile strain on the perovskite precursor phase with a pseudocubic lattice parameter of $a_{pc} = 0.381\,\mathrm{nm}$ (approximately +2.5%). This large tensile strain leads to a larger content of oxygen vacancies if compared to a relatively small compressive strain (approximately -0.5%) when grown onto $\mathrm{LaAlO_3}$ (LAO) single crystal [8]. In both cases a proper optimization process of the growth conditions is necessary to achieve bulk-like transport properties[9].

Moreover, stabilizing the Sr-doped $\mathrm{NdNiO_3}$ perovskite phase on STO substrate is challenging due to Sr-segregation issues and an unfavorable valence state of the Ni ions[10, 11]. These factors necessitate a delicate balance of growth parameters to mitigate epitaxial mismatches for both the perovskite precursors and IL phases. A novel approach to overcome these challenges involves the development of freestanding nickelate membranes, which are free from substrate-induced strain, using a wet etching method. This method includes growing the material onto a sacrificial layer, which is later removed via selective etching, allowing for the fabrication of oxide membranes while maintaining their structural integrity [12]. Additionally, utilizing water-soluble sacrificial layers $(\mathrm{Ca,Sr,Ba})_3\mathrm{Al_2O_6}$, which can be dissolved at room temperature without the use of any chemical pollutants, provides a versatile method to fabricate nickelate membranes [13]. The lattice parameter of these layers can be adjusted

from 0.382 nm (100% Ca) to 0.412 nm (100% Ba), thereby enhancing membrane quality and reducing crack formation[14, 15].

Here, we report on the fabrication of freestanding perovskite $NdNiO_3$ membranes using $(Sr,Ca)_3Al_2O_6$ sacrificial layers, and on the subsequent topotactic reduction after transferring onto silicon wafers to obtain IL $NdNiO_2$ membranes with good structural integrity. Very recently, superconducting membranes of infinite-layer nickelates were obtained by performing the topotactic reduction prior to transfer, which proves that it is indeed possible to grow the perovskite precursor phases onto specific sacrificial layers, perform topotactic reduction and then achieve a transfer of the superconducting flakes[16, 17]. The reduction of $NdNiO_3$ membranes proposed in this study aims to gather information about the feasibility of stabilizing the IL phase after transferring the membrane, which is then free from any substrate-induced effects. Our experimental approach allows membranes extending up to 5x5 mm^2 to be seamlessly transferred onto various substrates, yielding crack-free flakes of millimeter size. X-ray diffraction measurements have demonstrated that the membranes retain the crystalline quality of the original seed films. Furthermore, we demonstrate the two-fold potential of using a sacrificial layer to stabilize the IL phase via topotactic reduction of nickelate membranes: (1) we could perform the growth of the precursor nickelate onto substrates with an ideal lattice mismatch (*i.e.*, LAO), therefore limiting the formation of extended defects triggered by the strain accommodation highly relevant in the case of STO-grown samples; (2) we could obtain an important information about the substrate's influence on the IL stabilization, making a direct link with bulk preparation of IL nickelates.

II. RESULTS AND DISCUSSION

An important prerequisite for realizing freestanding crystalline membranes is the choice of the sacrificial layer, which must ensure a good lattice mismatch with both the target membrane layers and the substrate, while allowing for perfect etching selectivity. As an example, here, we report on our experience using $La_{0.825}Sr_{0.175}MnO_3$ (LSMO) as a potential sacrificial layer to fabricate $NdNiO_3$ (NNO3) membranes. Motivated by the fact that LAO single crystals are ideal substrates for the growth of nickelate thin films due to the minimal strain [18], we first optimized NNO3/LSMO//LAO heterostructures. Despite their high structural quality, we were unable to fabricate NNO3 membranes because the LSMO etchant (HCl+KI-

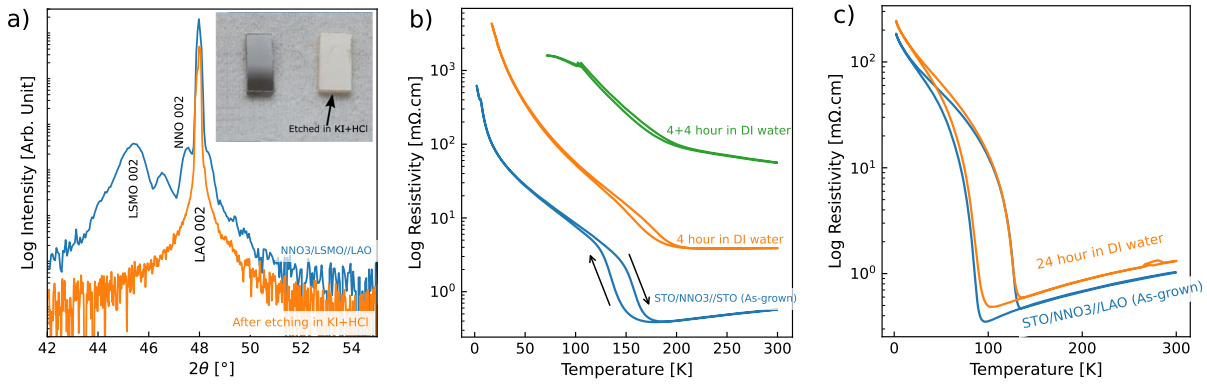

FIG. 1. a) $\theta - 2\theta$ symmetric scan of the 10 nm NNO3 layer on LSMO on LAO substrate before and after etching in a solution of 4 mg KI, 5 ml HCl (37%) + 200 ml H_2O, with an inset showing a photograph of a 10 nm NNO3 layer on an STO substrate before and after etching. b-c) Temperature-dependent resistivity of STO-capped NNO3 grown on STO and LAO substrates, respectively, before and after exposure to DI water.

based solution) was not selective, etching NNO3 similarly to LSMO. Figure 1a shows $\theta - 2\theta$ X-ray diffraction (XRD) patterns for the NNO3/LSMO//LAO heterostructure before and after approximately two hours of etching. The XRD pattern, characterized by Laue oscillations around the LAO (00l) peaks due to the perfect NNO3-LAO lattice mismatch, completely disappears after etching. This confirms the non-selectivity of the HCl+KI-based solution, which was also tested with a bare NNO3//STO sample. The photograph in the inset of Figure 1a shows NNO3//STO before and after etching, in which the NNO3 layer is completely removed. Similar results were obtained (not shown) even when the NNO3 layers were encapsulated between two 10 nm thick STO layers as a potential protection from direct contact with the LSMO etching solution.

To cope with this problem, we resorted to water-soluble sacrificial buffer layers already used in the literature to fabricate perovskite membranes [13]. These are particularly promising for the fabrication of nickelate membranes due to their good structural compatibility with nickelates. For example, $Ca_3Al_2O_6$ (CAO) has a cubic unit cell (space group $Pa\bar{3}$) with a lattice parameter of 1.526 nm, which closely matches the pseudocubic unit cells of both LAO and NNO3 ($a_{CAO} = 1.526 \sim 0.381 \times 4$ nm). Moreover, substituting Ca with Sr in specific ratios allows for tuning the CAO lattice parameter from $a/4 \sim 0.381$ nm for $Ca_3Al_2O_6$ to $a/4 \sim 0.396$ nm for $Sr_3Al_2O_6$ (SAO), which dissolves in deionized (DI) water much faster (in a

few minutes compared to approximately two days for CAO) due to the predominantly ionic Sr–O bonds [15]. This extended dissolution time necessitates studying the effect of DI-water on the functional properties of NNO3, as protonation effects have been shown to play a role on the related transport properties [19]. Figure 1b shows the temperature-dependence resistivity measurements for STO-capped NNO3 thin films before and after immersion in DI-water of various duration. It is seen that properly optimized NNO3 thin films grown onto STO are very sensitive to DI-water, and the usual hysteretic metal-to-insulator transition (MIT) with an onset temperature of approximately 140 K is significantly altered until the sample becomes fully insulating after eight hours of immersion. This behavior is absent when NNO3 is grown onto LAO substrates, where similar transport properties are observed even after one day in DI-water, as shown in Figures 1c. This compelling difference is most likely originating from the different strain state that the NNO3 thin films experience when grown onto STO (tensile) and LAO (slightly compressive) substrates which is found to affect the intrinsic content of oxygen vacancies [8]. To counteract the effect of DI-water on the fabricated membranes, we performed an oxygen post-annealing process as will be introduced later.

Epitaxial growth of the heterostructures

We used a pulsed laser deposition technique to grow NNO3-based heterostructures (HTs) using several sacrificial layers, such as $Sr_3Al_2O_6$ (SAO), $Ca_3Al_2O_6$ (CAO), and $Ca_2Sr_1Al_2O_6$ (CSAO) on both STO and LAO substrates (please refer to the Experimental Section for details). The NNO3 films directly grown onto the sacrificial layers appeared to exhibit modified transport properties, and the sacrificial layers became insoluble in water, suggesting that interdiffusion modifies the electronic and chemical properties of both layers. In addition, the use of LAO layers as a barrier to prevent interdiffusion (i.e., LAO/NNO3/LAO/CAO//LAO) resulted in interdiffusion between the LAO and CAO layers. Therefore, the 10 nm thick NNO3 films were encapsulated between two layers of STO, approximately 10–25 unit cells thick, which prevented potential interdiffusion of ions between the sacrificial layers and NNO3[20]. Reflection high-energy electron diffraction (RHEED) patterns taken after the growth of sacrificial, STO bottom, and NNO3 layers showed 2D streaky features, indicating clear layer-by-layer growth and an atomically flat surface, as illustrated in Figures 2a–b

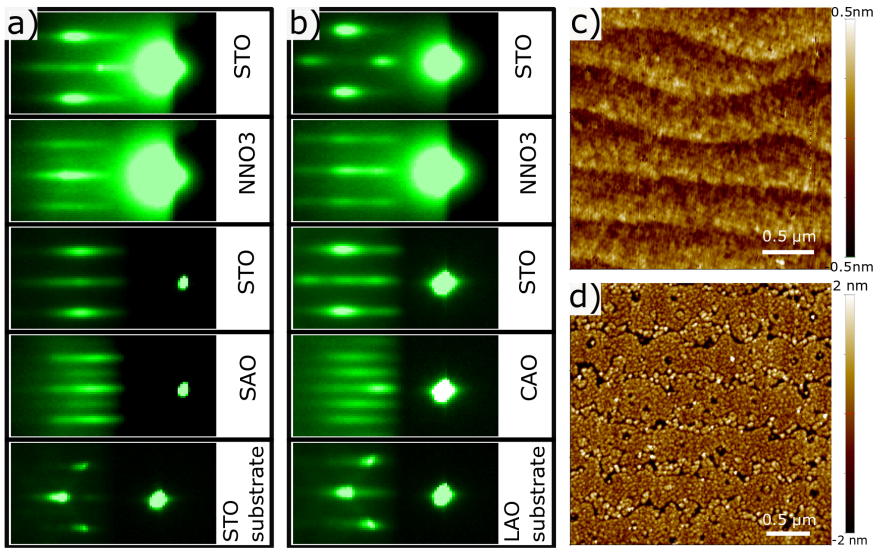

FIG. 2. a–b) RHEED diffraction patterns for SAO-STO and CAO-LAO HTs along the (001) direction of the substrates upon the completion of each layer's growth. The order of the RHEED images is from bottom to top, following the structure of the samples at each corresponding stage. c–d) AFM topography images for SAO-STO and CAO-LAO HTs acquired after the growth, respectively.

for the STO/NNO3/STO/SAO//STO and STO/NNO3/STO/CAO//LAO HTs, hereafter referred to as SAO-STO and CAO-LAO, respectively. Results obtained using the CSAO sacrificial layer are shown in Figures S1a–b. After the growth of the top STO layer, the RHEED pattern exhibited a mix of 2D streaks and 3D transmission spots, indicating that the surface had developed a partial 3D morphology. This was also confirmed by Atomic Force Microscopy (AFM) measurements, with root-mean-square (rms) surface roughness ranging from 0.2 nm to 0.7 nm, as shown in Figures 2c–d.

Figures 3a–b show the θ–2θ XRD symmetric scans of both the CAO-LAO and SAO-STO HTs. The clear diffraction peaks of the sacrificial layers and the STO/NNO3/STO HTs confirm that all layers are grown with good crystalline quality. The STO multipeak structure for the CAO-LAO HTs might be associated with a partial strain gradient, which was also observed for STO/NNO3/STO/CSAO//LAO (CSAO-LAO) HTs (see Figure S2a). Reciprocal space mapping presented in Figures 3c-d, acquired around the asymmetric 103 diffraction peak of the substrates, show that the SAO sacrificial layer is not fully in-plane strained to the STO; surprisingly, the subsequent layer of NNO3 exhibits the same in-plane

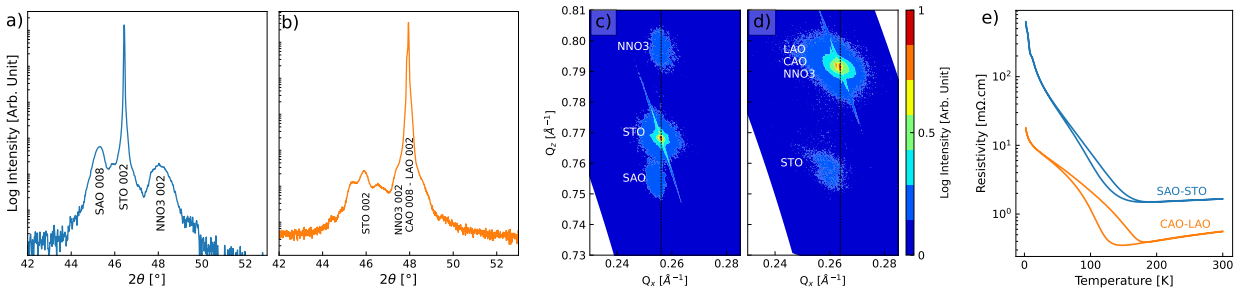

FIG. 3. Structural characterization of the as-grown heterostructures. $\theta-2\theta$ symmetric scans of the as-grown a) SAO-STO and b) CAO-LAO heterostructures. Reciprocal space maps around the STO and LAO 103 asymmetric diffraction peaks for the c) SAO-STO and d) CAO-LAO heterostructures. e) Temperature-dependent resistivity of both SAO-STO and CAO-LAO heterostructures.

lattice parameter as the STO substrate. For the CAO-LAO HTs, both the sacrificial layer and NNO3 are fully strained to the LAO, as expected from the good lattice mismatches, while the STO is partially relaxed. To attest to the quality of the NNO3 films, we also performed temperature-dependent resistivity, and as reported in Figure 3e, both HTs exhibit the characteristic features of perovskite nickelate thin films with metallic behavior at high temperatures followed by a hysteretic metal-to-insulator transition below approximately 150 K, with a resistance change of at least two orders of magnitude [21]. In particular, the CAO-LAO HT shows better metallic behavior, with an overall resistivity at 300 K lower than 1 mΩ·cm, and a larger hysteresis, likely resulting from the better lattice match with the LAO single crystal and the reduced internal strain state of the HTs, which leads to fewer extended defects and/or oxygen vacancies. On the other hand, the smaller hysteresis in SAO-STO HT, accompanied also by a modified curvature of the temperature-dependent resistivity curve, suggests that the large tensile strain imposed by the STO substrate, along with growth on the SAO sacrificial layer, may locally affect the electronic properties of NNO3[9], leading to lower quality membranes. Indeed, from the XRD of the NNO3 002 diffraction peak, we measured values around 48°, which is lower than the 48.5° usually measured for direct growth onto the STO substrates[10]. Overall, these results indicate that the sacrificial layers with the adjacently grown STO thin films do not affect the quality of the NNO3 thin films, which exhibit good epitaxial growth. It is worth mentioning that similar transport properties for NNO3 are measured for CSAO-LAO HTs, while STO/NNO3/STO/SAO//LAO (SAO-LAO) HTs resulted in a completely insulating behavior of the NNO3, even though the RHEED

patterns indicated 2D-like growth of the layers (see Figure S2c).

Epitaxial lift-off (membrane release)

Figure 4a–c schematically shows the process flow for fabricating freestanding membranes. First, water-soluble sacrificial layers are grown onto STO and/or LAO single crystals, followed by the growth of the STO/NNO3/STO heterostructure. A polymer support (PDMS), attached to a glass slide, is cut into pieces larger than the sample surface, and brought into conformal contact with the sample surface. Then, the stack of polymer and sample is immersed in DI-water to selectively etch the sacrificial layer. The etching time for the sacrificial layers varies from one to two hours for SAO, up to two days for CSAO and CAO. After verifying the complete etching of the sacrificial layer, the glass+PDMS+heterostructure stack is released from the substrate, then placed in contact with the recipient substrate (SiO_2/Si) using a transfer system with micrometer XYZ stages. The SiO_2/Si substrate had been previously ultrasonically cleaned in acetone and isopropyl alcohol. After annealing the entire stack in air at 70°C for 10 minutes to promote adhesion on the SiO_2/Si substrate, the

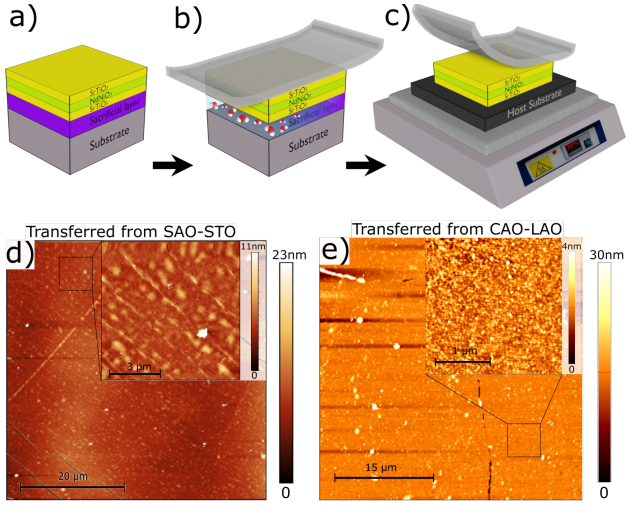

FIG. 4. a–c) Freestanding membranes fabrication process flow. a) Epitaxial growth of the sacrificial (water-soluble) layer and the STO/NNO3/STO heterostructure. b) Fixing the polymer support on sample surface and etching in de-ionized water. c) Transfer to the host substrate and peel-off of the polymer support. d-e) AFM topography images of the heterostructure transferred from SAO-STO and CAO-LAO respectively.

PDMS stamp is then carefully peeled off by raising the glass+PDMS support using one of the micrometer stages of our system.

Depending on the lattice parameters of the sacrificial layer and substrate, the resultant membranes exhibited different characteristics. The membranes obtained by dissolving SAO and CAO sacrificial layers were characterized by a complete transfer onto the polymer support, yet with notably different numbers and sizes of cracks. Membranes released from SAO-STO exhibited parallel micrometer-scale cracks in one direction, which were only visible by AFM, while the CAO-LAO membranes displayed fewer cracks having no particular direction, as shown in Figure 4d-e. Such differences in crack formation between these two types of membranes can be attributed to the strain state and number of defects; a low lattice mismatch between NNO3, CAO, and the LAO substrate permits coherent epitaxial growth of the films, which was confirmed by RSM measurements (see Figure 3c-d). On the other hand, membranes released from CSAO-LAO tended to bend upon themselves and curled into microscopic rolls, as shown in the SEM image of Figure S3c.

To further study the structural integrity of the freestanding membranes, we conducted XRD $\theta - 2\theta$ symmetric and asymmetric scans of the membranes transferred onto SiO_2(300 nm)/Si wafers. After transfer, the membranes were annealed for 3 hours at 300°C under an oxygen flow to mitigate possible protonation effects. In Figure 5a, we present the $\theta - 2\theta$

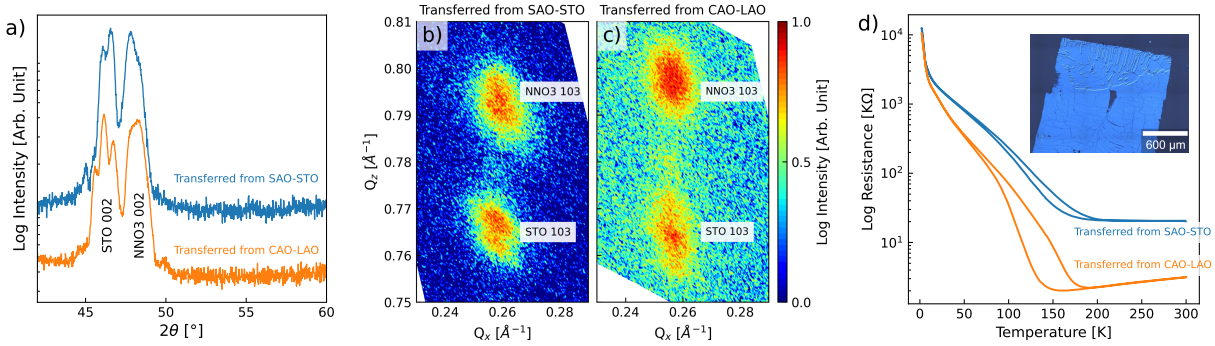

FIG. 5. a) $\theta - 2\theta$ scan and b–c) Reciprocal space maps around NNO3 and STO 103 diffraction peaks of the STO/NNO3/STO heterostructures transferred from SAO-STO and CAO-LAO, respectively. d) Temperature-dependent resistance of STO/NNO3/STO heterostructures membranes after transferring on to SiO2/Si wafer and annealing for 3 hours at 300°C under oxygen flow. Insets: optical image of the freestanding membrane on SiO2/Si substrate with micro Au-electrodes and Al wire bonds.

symmetric scan of STO/NNO3/STO heterostructure membranes transferred from SAO-STO and CAO-LAO HTs. It is seen that all membranes exhibit (002) diffraction peaks for STO and NNO3, similar to those of the as-grown HTs before release, confirming the conservation of crystalline integrity for both NNO3 and STO layers. The three side-by-side peaks observed in the STO layers, which have also been measured in other studies [16, 17], result from the Laue oscillations of the bottom and upper STO layers (Figure S4b), as confirmed by XRD simulations performed using a kinematic simulation MATLAB program[22]. The RSM measurements performed on the membranes showed that, after release, the three layers of the STO/NNO3/STO HTs remain epitaxially coupled, resulting in an equilibrium strain state, as shown in Figure 5b-c. The final strain of the layers in the membranes results from a trade-off between their elastic properties, thickness, and the initial strain withstanding during growth of the stack and assured by the choice of the substrate[23]. As a result of this process, in all membranes, the NNO3 layer is strained to the STO buffer layers, and conversely the STO layer is finely strained to NNO3. The higher applied strain by the STO layers, compared to NNO3, is likely due to their respective thicknesses, as the two STO layers are double the thickness of NNO3. Consequently, the NNO3 thin film grown onto LAO do not show the expected bulk values, but during release the in-plane lattice parameter is partially adjusted to the STO one. The lattice parameters and the calculated in-plane and out-of-plane strains in the membranes extracted from the RSM data are listed in Table I (see also Table S1).

In Figure 5d, we present the temperature-dependent resistance of the membranes, which were measured after the deposition of gold electrodes and aluminum wire bonding (see inset). The membranes preserved their transport properties that were shown in Figure 3e, with both the high-temperature metallic behavior and the low-temperature insulating phase, featuring a well-defined metal-to-insulator transition of the NNO3 layer and similar hysteresis as already reported for the grown HTs. Note that the difference in the magnitude of resistivity shown in Figure 3e and resistance shown in Figure 5d stems from the method by which the transport is measured. However, both display temperature-dependent resistance of the same order of magnitude when measured in a two-point contact configuration, as shown in Figure S8. These results are highly reproducible, as can be seen in the Figure S4a in supporting information.

TABLE I. Lattice parameters and strain states of the STO/NNO3/STO freestanding membrane heterostructures transferred from SAO-STO to CAO-LAO. Note: The strain state in the membranes depends on the thickness of the STO buffer layers; here, the STO thickness is ~ 10 nm.

Material	a-axis [Å]±0.01	c-axis [Å]±0.01	ip strain [%]	oop stain[%]
STO of SAO-STO	3.87	3.91	-0.9	0.13
NNO of SAO-STO	3.87	3.78	1.63	-0.74
STO of CAO-LAO	3.89	3.92	-0.38	0.51
NNO of CAO-LAO	3.89	3.76	2.15	-1.26

Topotactic reduction of the membranes

After the successful fabrication of the STO/NNO3/STO membranes, we performed a topochemical reduction by placing them in an evacuated silica tube sealed with a membrane-valve, where 0.5 g of CaH_2 powder was put in direct contact with them, as used in prior studies[10]. The process was optimised by a systematic series of steps, with $\theta - 2\theta$ scans and temperature-dependent resistance measurements performed ex situ after each step to assess the degree of topotactic reduction. A temperature of 240°C was found to be optimal for reduction, high enough to enable the reduction and low enough to avoid any damage to the membranes. In Figure 6, we present $\theta - 2\theta$ symmetric scans and temperature-dependent resistance measurements of two steps of the topotactic reduction process. After a first step of reduction, the NNO3(002) XRD diffraction peak considerably decreased in intensity for membranes obtained from SAO-STO HTs, while for CAO-LAO membranes, the XRD peak, still intense, began to shift towards higher 2θ values as expected for a proper stabilization of the IL phase. An additional step of reduction resulted in a complete shift to the typical 2θ value expected for IL films, for the membranes obtained from CAO-LAO HTs, with substantial intensity (Figure 6b). Notably, the $\theta - 2\theta$ symmetric scans, give the relevant information that the stabilization of the IL phase is obtained only in the case of membranes released from the CAO-LAO HTs while the ones obtained from the SAO-STO HTs practically decomposed, as demonstrated by the almost complete absence of the IL diffraction peak in Figure 6a. This disparity could be ascribed to intrinsic defects present in the related perovskite precursor phase, most likely linked to the large tensile strain that

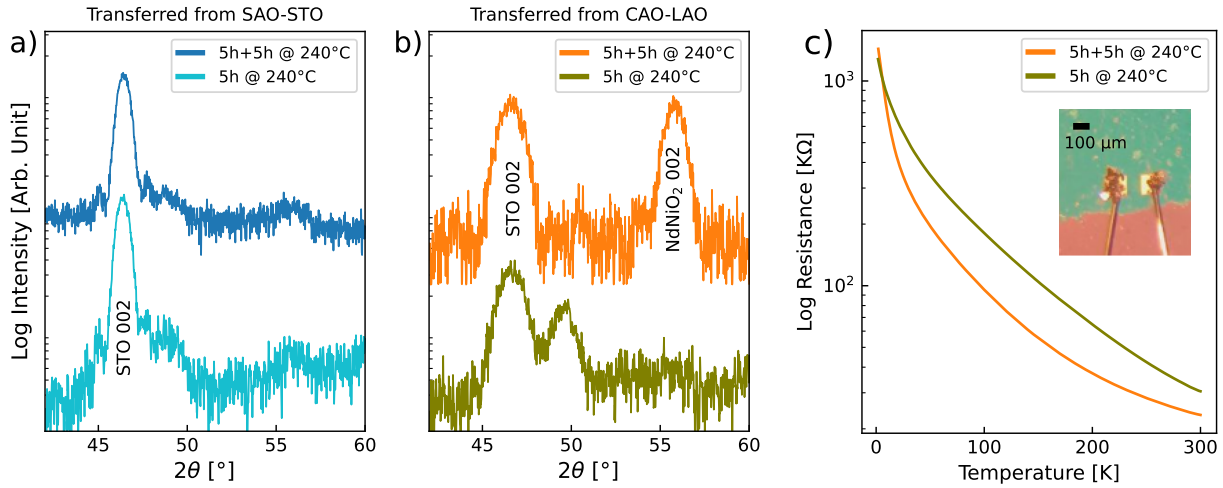

FIG. 6. a–b) $\theta - 2\theta$ symmetric scans of the STO/NNO3/STO heterostructure membranes after topochemical reduction for 5 hours at 240°C, followed by an additional 5 hours of reduction at the same temperature, for membranes transferred from a) SAO-STO and b) CAO-LAO. c) Temperature-dependent resistance of the freestanding infinite-layer membranes transferred from CAO-LAO; inset: optical microscope image of a reduced membrane after bonding.

NNO3 experiences during growth onto STO and the adjacent sacrificial layer. In particular, as already highlighted above, the membranes released from CAO-LAO HTs showed better metallic behavior and a larger hysteresis (Figure 5d), while from the Table I, we can note that only for CAO-LAO membranes the STO lattice parameter is closer to the bulk one, therefore exerting a lower compressive strain on the forming IL tetragonal crystal structure, if compared to the one obtained in the case of SAO-STO membranes.

Transmission electron microscopy observations of cross sections of the membranes transferred from CAO-LAO confirm their high crystalline quality as shown in Figure 7, although regions with Ruddlesden-Popper-type defects can be easily be recognized as already shown in literature for thin films and membranes Ref[17]. Their topotactic reduction is confirmed by both the observation of a reduced out-of-plane cell parameter, as seen in high-angular annular dark field (HAADF) images (Figure 7a), and the confirmation that the apical oxygen atoms have been removed, leaving the infinite-layer with oxygen only in the Ni-O planes, as deduced from integrated Differential Phase Contrast (iDPC) observations (Figure 7b).

Although both XRD patterns and TEM observations indicate the formation of a high crystalline quality for the IL phase obtained from CAO-LAO membranes, they showed insu-

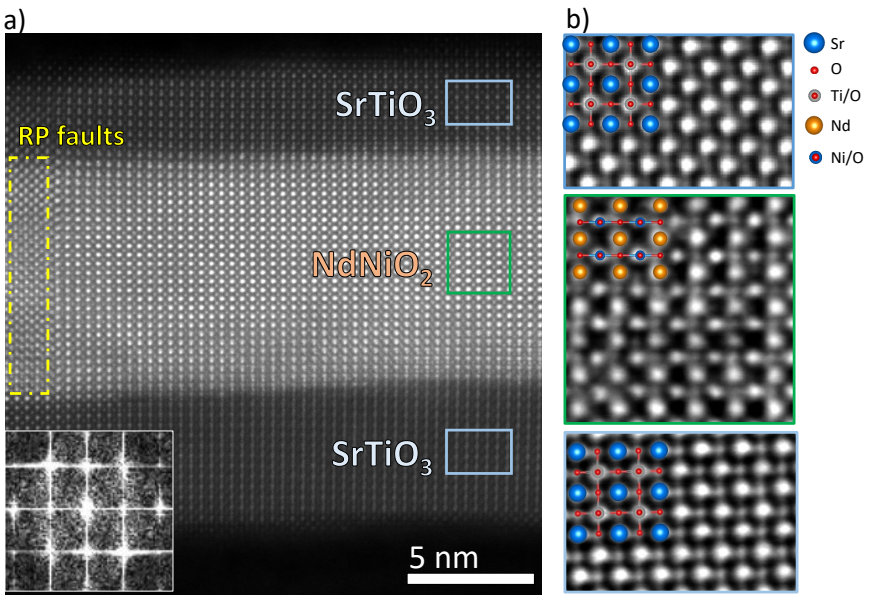

FIG. 7. a) The high-angle annular dark field (HAADF) STEM image obtained from the infinite-layer $NdNiO_2$ free-standing membrane transferred from CAO-LAO. The yellow dashed square outlines a region with a Ruddlesden-Popper fault. The fast-Fourier transform pattern obtained from the infinite-layer nickelate membrane is shown in the inset. The out-of-plane parameter is significantly lower than the in-plane one, thus confirming the infinite-layer nature of the membrane. b) Integrated Differential Phase Contrast (iDPC) image obtained from the central region of the membrane. The oxygen atoms are now seen along with the heavier species. The oxygen atoms are only seen in the Ni-O planes and not in the Nd-O planes, which again confirms the infinite-layer structure.

lating transport properties. This insulating behavior cannot be attributed to further cracks formation during the topotactic reduction process, since no additional crack formation was observed by optical microscopy and AFM as shown in Figure S6. On the other hand, from a structural point of view, we observed a decrease in the c-axis lattice parameter of the STO buffer layers after reduction, changing from 0.3920 nm to 0.3896 nm. This change indirectly indicates an increase in the in-plane lattice parameter of the STO layer, which thereby adapts itself to the a-axis of the forming IL-phase. Furthermore, the c-axis lattice parameter of STO buffer layers is observed to be modified compared to what is measured for the STO substrate, as shown in Figure S5. Finally, the fully insulating behavior of IL membranes, which is similar to what has been measured for bulk IL [6], points to the experimental fact

that a greater strain effect from the STO buffer layer (a substrate-like), is necessary to enable a more coherent stabilization of the IL phase with the expected transport properties.

To understand the feasibility of reducing the STO/NNO3/STO heterostructure in the presence of a sacrificial layer and LAO substrate, we performed topotactic reduction on a sample prior to transfer. Figure S7 shows θ-2θ symmetric scans and temperature-dependent resistivity of a CAO-LAO heterostructure before and after a two-step topochemical reduction. After the first reduction (5 hours at 240°C), a very small and broad peak appeared at the expected 2θ value for IL, which rather than transformation to IL may indicate a transformation towards intermediate and/or spurious phases accompanied also by an insulating temperature-dependent resistivity. Further reduction (2 hours at 240°C), resulted in no XRD peak at all with a further increase of the overall resistance, as indeed expected due to the large difference of the in-plane lattice parameters between LAO (3.79 Å) and IL-phase (3.92 Å).

CONCLUSION

We reported about the successful growth onto different substrates of epitaxial STO-encapsulated $NdNiO_3$ (NNO3) heterostructures with water-soluble $(Ca,Sr)_3Al_2O_6$ sacrificial layers. The as-grown HTs as well as the released membranes showed similar structural and transport properties, although, the overall strain relaxation during membrane formation rendered different lattice-parameters as shown in Table I. We demonstrated by TEM and XRD measurements that an infinite-layer phase could be properly stabilized from CAO-LAO HTs released membranes. The latter, nevertheless, displayed a fully insulating behaviour similarly to bulk. From our structural study it appeared clear that the STO buffer layers re-adjust their lattice parameters to the IL-phase one (*i.e.* a = 0.392 nm) during the topotactic reduction. Thus, not providing the optimal (compressive) strain to the IL-phase, which might be the necessary and sufficient condition to grant the ideal transport properties as observed in the case of IL nickelate thin films. Finally, our results highlight the key role played by the substrate-induced epitaxial strain on the formation of the nickelates IL phase. We are confident that the optimization of the sandwich material, either in its nature or thickness, will allow fine-tuning of the different strains and lead to freestanding nickelates IL membrane with expected transport and electronic properties.

III. EXPERIMENTAL

a. ***Epitaxial film fabrication:*** The epitaxial growth of NNO3-based HTs onto STO and LAO substrates was done by pulsed laser deposition using a 248 nm KrF excimer laser, utilizing single-crystal targets from Toshima Manufacturing CO LTD. The STO substrates were prepared by etching in an NH_4F-buffered HF solution, then annealed for 2 hours at 950°C in air to obtain a well-defined TiO_2-terminated step-terraced surface. In contrast, the LAO substrates were annealed for 10 hours at 1000°C to achieve an AlO_2-terminated step-terraced surface. Prior to growth, each substrate was pre-annealed for 1 hour at 800°C under a pressure of 0.3 mbar in an oxygen flow to ensure a sharp step-and-terrace surface. Approximately 20 nm $Sr_3Al_2O_6$ (SAO), $Ca_3Al_2O_6$ (CAO), and $Ca_2Sr_1Al_2O_6$ (CSAO) sacrificial layers were grown on top of the STO(LAO) (001) substrates at a substrate temperature of 800°C and an oxygen partial pressure of $P_{O_2} = 1.2 \times 10^{-5}$ mbar, using a laser fluence of 1.2 J/cm^2 and a 1×1.4 mm^2 laser spot size on the targets. The bottom STO buffer layers (6-10 nm) were grown on the sacrificial layers under the same growth conditions. Next, the 10 nm NNO3 layers were grown on top of the STO buffer layers at a temperature of 675°C and $P_{O_2} = 0.3$ mbar, with a laser fluence of 3.3 J/cm^2 and a 1×1.4 mm^2 laser spot size. Finally, the top STO layer was grown at a T of 575°C and $P_{O_2} = 0.3$ mbar, with a laser fluence of 1.2 J/cm^2 and a 1×1.4 mm^2 laser spot size.

b. ***Transfer of freestanding membranes:*** A flexible polymer (PDMS) was adhered to the heterostructure surface (Figure 4b), and then the assembly was immersed in room-temperature de-ionized water to dissolve the sacrificial layers. After dissolution, the freestanding membranes were transferred to SiO_2/Si substrates by placing and pressing the membrane with PDMS onto the heated (70°C) silicon wafer (Figure 4c). By peeling off the PDMS support, the membranes remain on the wafers and detach from the support.

c. ***Characterization:*** The surface morphology of the samples was acquired using a Park XE7 (Park System) atomic force microscope (AFM) in true non-contact mode. The XRD data were collected using Bruker D8 Advance and PANalytical X'Pert Pro diffractometers with a Cu-Kα radiation source (0.1154056 nm). The transport properties of the heterostructures on the single-crystal substrates were studied using a Dynacool system (Quantum Design) and measured using the van der Pauw method on 5×5 mm^2 samples by applying current amplitudes of 10 μA. To measure the transport of the transferred membrane flakes,

Au electrodes were first fabricated by photolithography; then, the electrodes were bonded, and the transport measurements were conducted in two-point contact mode. The high-angle annular dark-field (HAADF) images were acquired in a double-corrected Thermofisher Spectra 300 (S)TEM micrsocope operated at 300 KV, using a convergence semi-angle of around 20 mrad. The oxygen sublattice was imaged by means of integrated differential phase contrast (iDPC) imaging using the segmented Panther detector from Thermofisher and a camera length of around 145 mm. For the STEM experiments, a cross sectional view lamella was prepared using a focused ion beam (FIB) Helios 5 UX from Thermofisher.

ACKNOWLEDGMENTS

This work was funded by the French National Research Agency (ANR) through the ANR-JCJC FOXIES ANR-21-CE08-0021. This work was also done as part of the Interdisciplinary Thematic Institute QMat, ITI 2021 2028 program of the University of Strasbourg, CNRS and Inserm, and supported by IdEx Unistra (ANR 10 IDEX 0002), and by SFRI STRAT'US project (ANR 20 SFRI 0012) and EUR QMAT ANR-17-EURE-0024 under the framework of the French Investments for the Future Program. It was also supported by France 2030 government investment plan managed by the French National Research Agency under grant reference PEPR SPIN – [SPINMAT] ANR-22-EXSP-0007. The authors thank the PLD, XRD, MEB-CRO, TEM, and MagTransCS platforms of the IPCMS. D. Pesquera and K.Cordero acknowledge Grant No. PID2022-140589NB-I00 funded by MCIN/AEI/10.13039/501100011033. D. Pesquera acknowledges funding from 'la Caixa' Foundation fellowship (ID 100010434). The ICN2 is funded by the CERCA programme / Generalitat de Catalunya and by the Severo Ochoa Centres of Excellence Programme, funded by the Spanish Research Agency (AEI, CEX2021-001214-S). Authors acknowledge the use of instrumentation financed through Grant IU16-014206 (METCAM-FIB) to ICN2 funded by the European Union through the European Regional Development Fund (ERDF), with the support of the Ministry of Research and Universities, Generalitat de Catalunya.

Supporting information: Freestanding perovskite and infinite-layer nickelate membranes

Hoshang Sahib[1], Laurent Schlur[1], Bernat Mundet[2], Kumara Cordero[2], Nathalie Viart[1], David Pesquera[2], and Daniele Preziosi[1],

[1] Université de Strasbourg, CNRS, IPCMS UMR 7504, F-67034 Strasbourg, France.

[2] Catalan Institute of Nanoscience and Nanotechnology, ICN2 Campus UAB 08193 Bellaterra, Barcelona, Spain

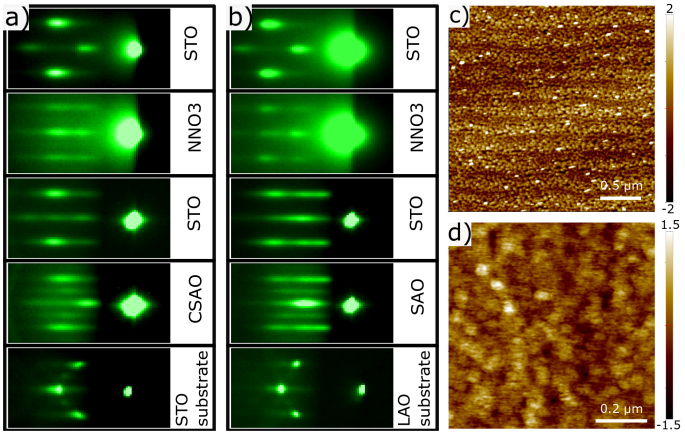

FIG. S1. a–b) RHEED diffraction patterns for CSAO-LAO and SAO-LAO heterostructures along the (001) direction of the substrates upon the completion of each layer's growth. c-d) AFM topography images of CSAO-LAO and SAO-LAO HTs acquired after the growth, respectively.

TABLE S1. Lattice parameters and strain states of a STO(3nm)/NNO3(10nm)/STO(3nm) free-standing membrane transferred from CAO-LAO.

Material	a-axis [Å]±0.01	c-axis [Å]±0.01	ip strain [%]	oop stain[%]
NNO of CAO-LAO	3.83	3.79	0.6	-0.48

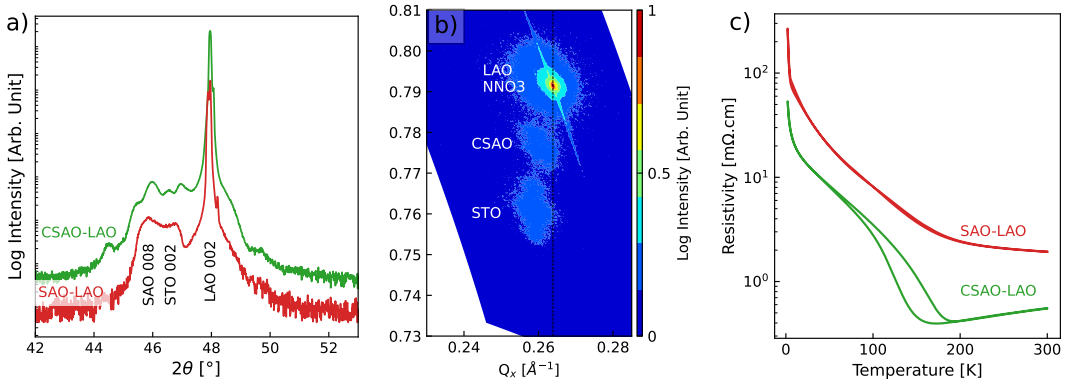

FIG. S2. a) $\theta-2\theta$ scans of the as-grown CSAO-LAO and SAO-LAO heterostructures. b) Reciprocal space map around the LAO 103 asymmetric diffraction peak for the CSAO-LAO heterostructure. c) Transport measurements of the as-grown CSAO-LAO and SAO-LAO heterostructures.

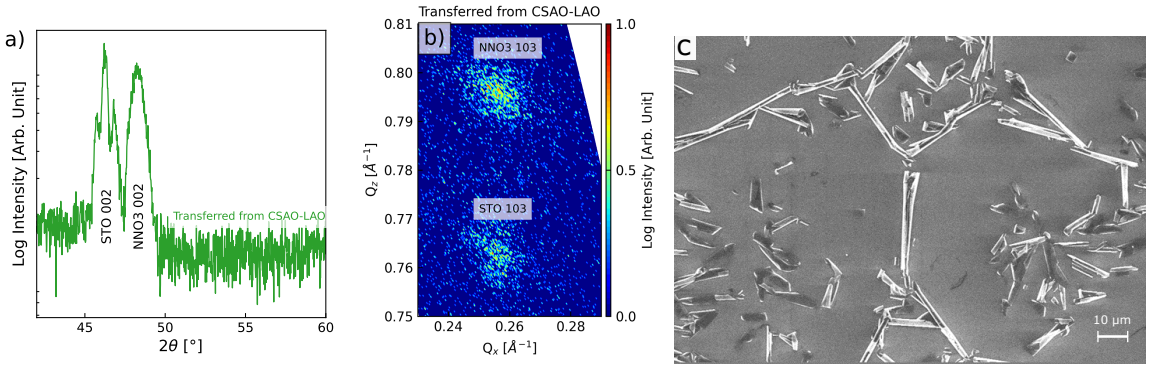

FIG. S3. a) $\theta-2\theta$ symmetric scan, b) Reciprocal space map around NNO3 and STO 103 diffraction peak, and c) SEM image of the STO/NNO3/STO heterostructure transferred from CSAO-LAO.

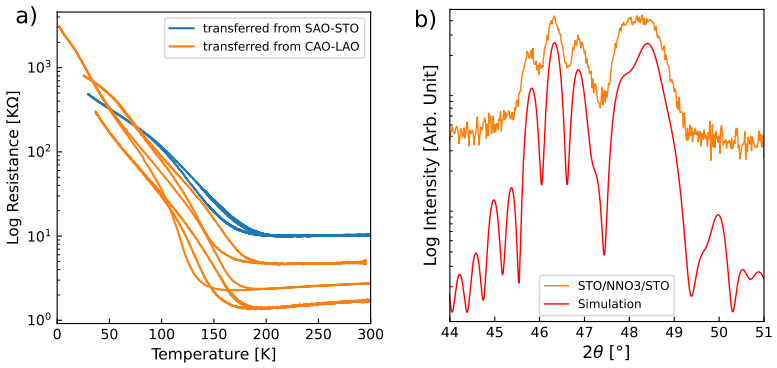

FIG. S4. a) Temperature-dependent resistance measurements of as-grown CAO-LAO and SAO-STO heterostructures for multiple membrane samples, b) $\theta - 2\theta$ symmetric scans of STO/NNO3/STO heterostructure transferred from CAO-LAO and corresponding simulation using lattice parameters from Table 1.

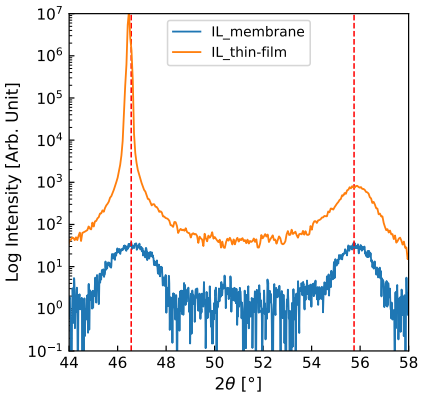

FIG. S5. $\theta - 2\theta$ symmetric scans of infinite-layer stabilized in the form of a thin film (in orange) and stabilized in the form of a membrane (in blue).

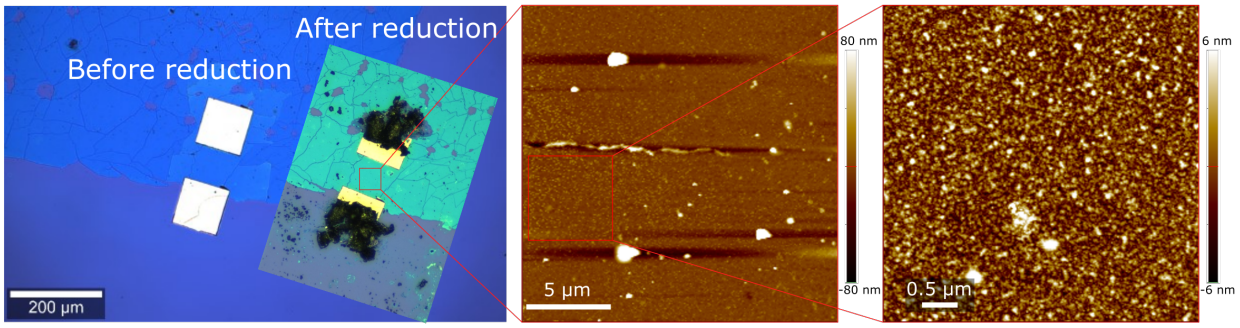

FIG. S6. Optical and AFM topography image of CAO-LAO membranes before and after topotactic reduction

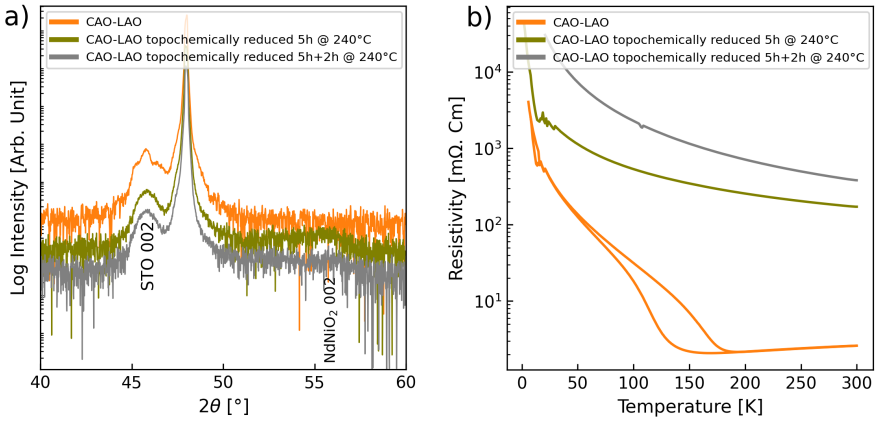

FIG. S7. a) $\theta - 2\theta$ symmetric scans and b) Temperature-dependent resistivity of a CAO-LAO heterostructure, before and after topochemical reduction for 5 hours at 240°C, followed by an additional 2 hours of reduction at the same temperature.

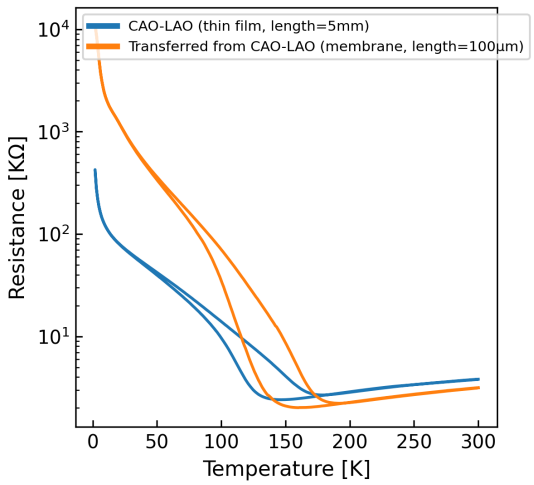

FIG. S8. Temperature-dependent resistance of a CAO-LAO heterostructure in thin film and membrane form, measured in two-point contact configuration.

[1] V. I. Anisimov, D. Bukhvalov, and T. M. Rice, Physical Review B **59**, 7901 (1999).

[2] A. M. Oleś, K. Wohlfeld, and G. Khaliullin, Condensed Matter **4**, 46 (2019).

[3] D. Li, K. Lee, B. Y. Wang, M. Osada, S. Crossley, H. R. Lee, Y. Cui, Y. Hikita, and H. Y. Hwang, Nature **572**, 624 (2019).

[4] M. Osada, B. Y. Wang, B. H. Goodge, K. Lee, H. Yoon, K. Sakuma, D. Li, M. Miura, L. F. Kourkoutis, and H. Y. Hwang, Nano letters **20**, 5735 (2020).

[5] S. Zeng, C. Li, L. E. Chow, Y. Cao, Z. Zhang, C. S. Tang, X. Yin, Z. S. Lim, J. Hu, P. Yang, et al., Science advances **8**, eabl9927 (2022).

[6] Q. Li, C. He, J. Si, X. Zhu, Y. Zhang, and H.-H. Wen, Commun. Mater. **1**, 16 (2020).

[7] M. A. Hayward and M. J. Rosseinsky, Solid State Sciences **5**, 839 (2003), international Conference on Inorganic Materials 2002.

[8] Q. Guo, S. Farokhipoor, C. Magén, F. Rivadulla, and B. Noheda, Nature Communications **11**, 2949 (2020).

[9] D. Preziosi, A. Sander, A. Barthélémy, and M. Bibes, AIP Advances **7** (2017).

[10] G. Krieger, A. Raji, L. Schlur, G. Versini, C. Bouillet, M. Lenertz, J. Robert, A. Gloter, N. Viart, and D. Preziosi, Journal of Physics D: Applied Physics **56**, 024003 (2022).

[11] K. Lee, B. H. Goodge, D. Li, M. Osada, B. Y. Wang, Y. Cui, L. F. Kourkoutis, and H. Y. Hwang, APL Materials **8**, 41107 (2020).

[12] D. Pesquera, A. Fernández, E. Khestanova, and L. W. Martin, Journal of Physics: Condensed Matter **34**, 383001 (2022).

[13] D. Lu, D. J. Baek, S. S. Hong, L. F. Kourkoutis, Y. Hikita, and H. Y. Hwang, Nature Materials **15**, 1255 (2016).

[14] F. M. Chiabrera, S. Yun, Y. Li, R. T. Dahm, H. Zhang, C. K. Kirchert, D. V. Christensen, F. Trier, T. S. Jespersen, and N. Pryds, Annalen der Physik **534**, 2200084 (2022).

[15] A. Prodjosantoso, B. J. Kennedy, and B. A. Hunter, Australian Journal of Chemistry **53**, 195 (2000).

[16] S. Yan, W. Mao, W. Sun, Y. Li, H. Sun, J. Yang, B. Hao, W. Guo, L. Nian, Z. Gu, et al., Advanced Materials , 2402916 (2024).

[17] Y. Lee, X. Wei, Y. Yu, L. Bhatt, K. Lee, B. H. Goodge, S. P. Harvey, B. Y. Wang, D. A.

Muller, L. F. Kourkoutis, et al., arXiv preprint (2024).

[18] S. Catalano, M. Gibert, J. Fowlie, J. Íñiguez, J.-M. Triscone, and J. Kreisel, Reports on Progress in Physics **81**, 046501 (2018).

[19] H. Chen, M. Dong, Y. Hu, T. Lin, Q. Zhang, E.-J. Guo, L. Gu, J. Wu, and Q. Lu, Nano Letters **22**, 8983 (2022).

[20] D. J. Baek, D. Lu, Y. Hikita, H. Y. Hwang, and L. F. Kourkoutis, APL Materials **5** (2017).

[21] J. Torrance, P. Lacorre, A. Nazzal, E. Ansaldo, and C. Niedermayer, Physical Review B **45**, 8209 (1992).

[22] C. Lichtensteiger, Journal of applied crystallography **51**, 1745 (2018).

[23] D. Pesquera, E. Parsonnet, A. Qualls, R. Xu, A. J. Gubser, J. Kim, Y. Jiang, G. Velarde, Y.-L. Huang, H. Y. Hwang, et al., Advanced Materials **32**, 2003780 (2020).